

Two-body relaxation in the EMRI-TDE disk model for Quasi Periodic Eruptions

Chiara Maria Allievi,¹ Luca Broggi^{1,2} Alberto Sesana,^{1,2} and Matteo Bonetti^{1,2,3}

¹ Dipartimento di Fisica “G. Occhialini”, Università degli Studi di Milano-Bicocca, Piazza della Scienza 3, I-20126 Milano, Italy

² INFN, Sezione di Milano-Bicocca, Piazza della Scienza 3, I-20126 Milano, Italy

³ INAF - Osservatorio Astronomico di Brera, via Brera 20, I-20121 Milano, Italy

Received XXX; accepted YYY

ABSTRACT

Quasi Periodic Eruptions (QPEs) are luminous bursts of soft X-rays recently discovered in galactic nuclei. They repeat on timescales of hours to weeks, superimposed to an otherwise stable quiescent X-ray level, consistent with emission from a radiatively efficient accretion flow around relatively low-mass massive black holes (MBHs). Although their physical origin is still debated, their quasi-periodicity naturally arises within the ‘impact model’, in which the X-ray bursts are generated by the interaction between a stellar black hole (sBH) or a star in a close orbit around the central MBH and the accretion disk formed by a tidal disruption event (TDE). While this model is consistent with the phenomenology of QPEs, it remains unclear whether such specific physical configurations are sufficiently common to explain the observed QPE number density. We present the first end-to-end quantitative calculation of the expected QPE rate and abundance within the framework of the impact model. To this purpose, we combine the rates of TDEs and extreme mass-ratio inspirals (EMRIs) around MBHs spanning a range of masses. We employ the public code PHASEFLOW to simulate seven systems with MBH masses between $10^5 M_\odot$ and $10^8 M_\odot$, each surrounded by a three-component population: one composed of $1 M_\odot$ stars, and two consisting of sBHs with masses of $10 M_\odot$ and $40 M_\odot$. Based on the emission constraints available in the literature, we restrict to sBH EMRIs on prograde orbit with eccentricity $e < 0.5$ and inclination $i < 20^\circ$ with respect to the accretion disk. For stellar EMRIs the constraints instead arise from the requirement that the star avoid tidal disruption. We find that the predicted QPE number density spans the range 10^{-12}Mpc^{-3} to 10^{-6}Mpc^{-3} , depending on the assumed orbital period interval and on the adopted eccentricity and inclination thresholds. QPEs generated by stellar EMRIs can reach number densities comparable to those inferred from current observations. In contrast, imposing the orbital constraints required for the sBH channel significantly suppresses the number of observable events, resulting in abundances approximately three orders of magnitude lower than in the stellar case. If the eccentricity and inclination constraints are relaxed, sBH-driven QPEs become compatible with the lower bound of the observationally inferred range.

Key words. galaxies:active – galaxies:nuclei – quasars:supermassive black holes – X-rays:bursts – Black hole physics – Relativistic processes

1. Introduction

X-ray quasi-periodic eruptions (QPEs) are an extreme and rather enigmatic phenomenon identified in the last decade (Miniutti et al. 2019). These signals have luminosities up to 10^{43}erg/s , a typical duration of one/few hours, and exhibit recurrence timescales around ten times longer. These eruptions are associated with fast spectral transitions between a cold and a warm phase in the accretion flow around a low-mass MBH.

Following their discovery, QPEs have been observed so far from the nuclei of other eleven galaxies (Giustini et al. 2020; Chakraborty et al. 2021; Arcodia et al. 2021; Quintin et al. 2023; Arcodia et al. 2024; Nicholl et al. 2024; Guolo et al. 2024; Chakraborty et al. 2025; Hernández-García et al. 2025).

The nature of the host galaxy is still under investigation. Half of them may be relatively low-mass post-starburst galaxies, a population that might be a preferential host for observed tidal disruption events (TDEs), (Miniutti et al. 2019; Chakraborty et al. 2021; Giustini et al. 2020; Arcodia et al. 2021; Guolo et al. 2024). Despite very little X-ray obscuration, none of the QPE galaxies show the typical optical or UV broad emission lines associated with unobscured, type I active galactic nuclei (AGNs), although the observed narrow-lines suggest the pres-

ence of an ionizing AGN-like continuum (Wevers et al. 2022), possibly suggesting past AGN activity.

The mechanism producing QPEs is uncertain, but most models involve accretion disks around massive black holes (MBHs), either modeling their instabilities (Pan et al. 2022; Śniegowska et al. 2023; Kaur et al. 2023) or their interaction with a stellar object piercing through it (Dai et al. 2010; Xian et al. 2021; Linial & Metzger 2023; Franchini et al. 2023a). It has been suggested that such a disk could be produced following a TDE (Linial & Metzger 2023; Kaur et al. 2023), indicating that a possible connection may exist between TDEs and QPEs. Indeed, two known QPE sources show long-term decays in quiescent luminosity consistent with TDEs (Miniutti, G. et al. 2023; Arcodia et al. 2024), and four observed TDEs have exhibited X-ray flares resembling individual QPE eruptions (Chakraborty et al. 2021; Quintin et al. 2023; Nicholl et al. 2024; Chakraborty et al. 2025). While TDEs are expected to occur in only about one out of every 10,000 galaxies, their detection in roughly half of the galaxies hosting QPEs suggests that such a connection might not be coincidental.

In this work we focus on the model for which the interaction between a star or a sBH and a TDE accretion disk gives

rise to QPEs. Specifically, we build upon the results of Franchini et al. (2023b), who modeled successive passages of QPEs within the sBH EMRI–TDE disk framework, and we extend this model by also considering interactions involving stars. We present the derivation of the number density of QPEs in the universe—referred to as the QPE volumetric abundance—to assess whether our theoretical predictions are consistent with observational estimates.

The paper is organized as follows. In Sec 2 we review the aspects of the theory relevant to our model of the QPEs origin and we present the theoretical reasoning behind the computation of the cosmic QPE volumetric abundance. In Sec 3 we present the simulations of the Nuclear Star Clusters (NSCs) we have taken into consideration and the implementation of the computation of the EMRI and TDE rates. In Sec 4 we explain the calculations behind the cosmic QPE volumetric abundance. Finally in Sec 5 we present the results of our work, so that we can discuss them in Sec 6 and draw our conclusions in Sec 7.

2. Disk Impact Model

In the model we consider, QPEs are produced by the collisions between a TDE accretion disk and a compact orbiter¹ (CO). Considering the scale of the system, the orbiter is typically undergoing an extreme mass-ratio inspiral (EMRI) around a MBH at the center of a galaxy (see Figure 1), as its motion is dominated by gravitational waves (GWs) emission. When the orbiter pierces the accretion disk, it strips some of its mass, which expands forming two bubbles: one on each side of the impact. Because of the expansion, the bubbles cool until they become optically thin and start emitting electromagnetic radiation. Since EMRIs can have semi-major axes entirely within the radial extent of the TDE disk, they periodically intersect the disk with a recurrence timescale that can match the observed timing of QPE bursts, including small differences among subsequent passages (Franchini et al. 2023a).

As sBHs do not have a proper physical surface, their cross section with the gas in the disk is set dynamically as the Bondi radius, i.e. $R = GM/(v_{\text{rel}}^2 + v_{\text{sound}}^2)$ (Bondi 1952). This implies some constraints on the EMRI orbit to reproduce the luminosities of QPEs, specifically the relative velocity between the sBH and the gas should be small for a sufficiently large radius. This translates into constraints on the orbital parameters, i.e. on the orbital eccentricity e and the inclination i of the orbital plane with respect to the disk: the eccentricity must be small to moderate ($e \lesssim 0.5$) and the inclination small ($i \lesssim 20^\circ$) (Franchini et al. 2023a; Chakraborty et al. 2024).

If the orbiter is a main sequence star, the impact radius is naturally set by the physical radius of the star. Therefore, the only constraint on the orbital properties arise from the stellar structure: the pericentre distance r_p of the EMRI must be larger than the tidal radius r_t , which encloses regions where the star is torn apart by the tidal field of the MBH. This requires $e < 1 - r_t/a$.

We estimate the abundance of QPE sources in the galactic population starting from the expected number of EMRI+TDE disk pairs in a single galactic nucleus. We assume that the compact orbiter is in place because of the combined effect of two-body relaxation and GW emission. In fact, weak scatterings can deflect the orbiters on low angular momentum orbits, where

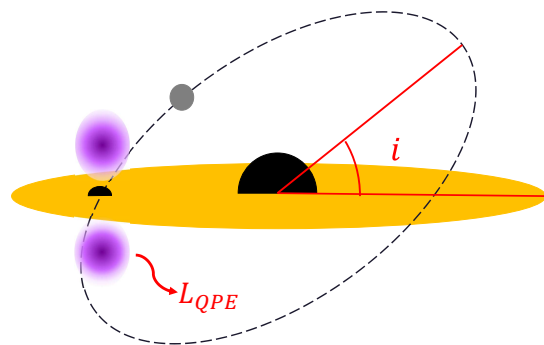


Fig. 1: Schematic representation of the QPE disk-impact model. The central big black dot represents the MBH, the small gray dot represents the compact orbiter, either a sBH or a star, the yellow area represents the TDE accretion disk, and the dashed line represents the EMRI trajectory. The angle between the disk and the EMRI orbital plane is the inclination i . The violet bubbles represent the stripped mass that expands both above and below the disk after the impact. As soon as the bubbles become optically thin, they emit electromagnetic radiation (L_{QPE})

GWs emitted at periastron binds them to the central MBH initiating the slow GW driven adiabatic inspiral defining an EMRI.

The number of compact orbiters N_{CO} in the GW dominated region is estimated as the product between the rate at which orbiters enter this region of phase space and the coalescence time; this number must account for eccentricity and inclination constraints. The number N_{disk} of TDE disks expected around the MBH is estimated as the product of the rate of stellar disruptions and the lifetime of the disk. The product $N_{\text{CO}} \times N_{\text{disk}}$ gives the expected number of potential QPE sources in a given galactic nucleus. As this number is usually smaller than unity, we interpret it as the probability of observing an active QPE source when observing a galactic nucleus.

2.1. TDEs and EMRIs from two-body relaxation

Dynamical interactions within NSCs can drive stellar objects onto very tight orbits around the central MBH. Through this mechanism, some objects are driven either to plunge directly into the MBH, to enter an EMRI phase, or, if they are not compact enough to survive, to undergo a TDE. Specifically, the large, finite number of objects in NSCs induces small deviations from the smooth average potential of the system. As a consequence, the orbital parameters of a stellar object are subject to a Brownian motion known as two-body relaxation. The leading effect is the accumulation of distant two-body encounters between the considered stellar object and each of the others. Considering the entire stellar population, the distribution of orbital parameters – that in spherical symmetry can be identified with specific energy and specific angular momentum – can be shown to evolve according to a diffusion-advection equation (the orbit averaged Fokker-Planck equation). Its coefficients are determined by the dynamics of two-body relaxation (Spitzer 1987).

It is possible to modify the Fokker-Planck equation to account for disruptive processes like tidal disruptions or gravita-

¹ With “compact orbiters” we consider every object around the SMBH outside its tidal disruption radius or its loss cone.

tional captures according to the loss cone theory². Loss cone phenomena are included by assuming an instantaneous disruption at the pericentre when it is smaller than a critical value r_{LC} , which can be treated with modified boundary conditions for the equation (Cohn & Kulsrud 1978).

The Brownian motion of stars in angular momentum is generally faster than that in energy (especially for very eccentric orbits); an approximate description of relaxation is based on decoupling the two processes. One can use a simplified evolution equation for the distribution in energy (the ergodic Fokker-Planck equation), and assume at any instant the relaxed profile in angular momentum. The latter is generally approximated with the nearly-radial, steady-state profile induced by loss cone disruptions at fixed energy (Cohn 1979; Merritt 2013; Vasiliev 2017; Stone et al. 2020).

2.1.1. TDEs and their disk

A star can be tidally disrupted by the MBH if it enters a critical radius (Hills 1975; Rees 1988; Phinney 1989). This distance is known as the tidal disruption radius r_t , and encloses the region in space where the tidal forces of the MBH overcome the self-gravity of a star, so that the latter is ripped apart. For a star of mass M_\star and radius R_\star it can be estimated as (Hills 1975)

$$r_t = \eta_\star \left(\frac{M_\bullet}{M_\star} \right)^{1/3} R_\star \quad (1)$$

where the form factor $\eta_\star \simeq 1$ depends on the internal structure of the star and possibly the eccentricity of the orbit. For stars, we assume loss cone events to happen with $r_{\text{LC}} = r_t$, with $\eta_\star = 1$.

We assume that every star penetrating the tidal radius is disrupted by the MBH and forms an accretion disk. Simulations show that the stellar debris of a TDE follows a range of trajectories, with some of the material becoming unbound and escaping. Conversely, the bound debris return to the pericenter on highly eccentric orbits, possibly self-interacting because of relativistic precession and orbital dynamics. These collisions dissipate energy and facilitate the circularization of the debris, leading to the gradual formation of the accretion disk (Dai et al. 2010; Shen & Matzner 2014; Bonnerot & Lu 2020; Curd 2021). This disk is the central engine powering the long term electromagnetic emission of a TDE, emitting radiation across multiple wavelengths as the material spirals inward and is accreted onto the black hole (Lodato & Rossi 2010; Lodato et al. 2015; Mummery & Balbus 2020). We assume a disk lifetime τ_{disk} of 10 years, consistent with the typical outcomes of simulations (Bonnerot et al. 2021; Piro & Mockler 2024).

2.1.2. EMRIs

An EMRI can form when two-body relaxation brings a stellar object into an orbit so close to the central MBH, that the emission of GWs dominates over relaxation, driving the object to coalescence.

The timescale for two-body relaxation t_{rlx} is set by the time it needs to change the angular momentum squared J^2 of an orbit by the order of itself. By defining eccentricity as $J^2/J_c^2 \equiv 1 - e^2$,

² The name loss cone comes from the shape spanned by the velocity vectors that, at a given location in space, are tangent to orbits penetrating within a certain distance. The distance enclosing orbits leading to disruptions, or losses, is known as the loss cone radius.

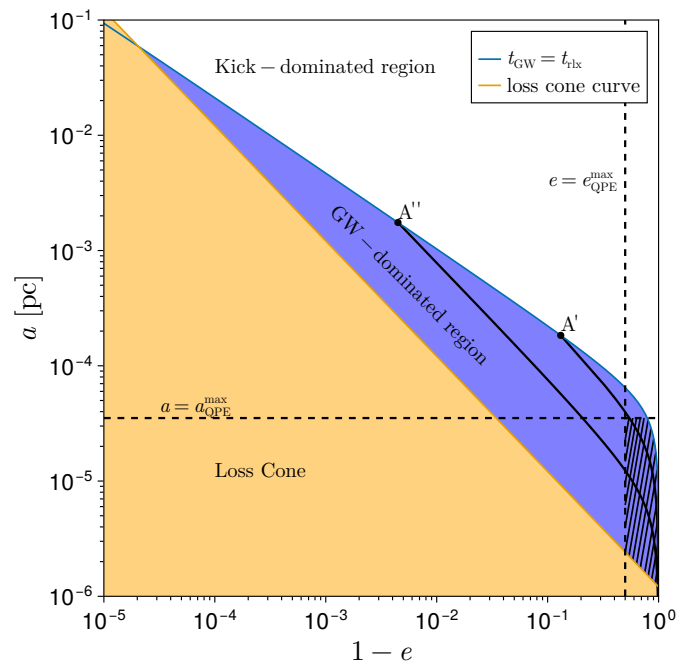


Fig. 2: Trajectories of EMRIs dominated by GW emission. In the blue region the gravitational-wave timescale t_{GW} is shorter than the relaxation timescale t_{rlx} ; the orange area encloses plunging orbits; the white area encloses orbits dominated by two-body relaxation. The shaded area encloses observable QPEs, that are determined by two parameters in our work: the maximum semi major axis $a_{\text{QPE}}^{\text{max}}$ (horizontal, dashed) and the maximum eccentricity $e_{\text{QPE}}^{\text{max}}$ (vertical, dashed). The black curves show the trajectory of sBHs that form EMRIs from Point A' and A'' and become observable QPEs. In this case, $M_\bullet = 3 \times 10^6 M_\odot$, $M_{\text{CO}} = 40 M_\odot$.

where $J_c(E)$ is the angular momentum of the circular orbit with energy E , one can write

$$t_{\text{rlx}} = \frac{1 - e^2}{\mathcal{D}(E)}, \quad (2)$$

where \mathcal{D} is the diffusion coefficient determined by two-body relaxation and depends only on the orbital energy E . We opted for this definition of the eccentricity e as it extends the Keplerian estimate to non-elliptical orbits influenced by the stellar potential.

To estimate the timescale of GWs emission, we consider the smallest between the time required to change $1 - e^2$ and a . The shortest is always $-a/\dot{a}_{\text{GW}}$, that for the typically eccentric loss cone orbits can be estimated as (Peters 1964):

$$t_{\text{GW}} = \frac{12 \sqrt{2}}{85} \frac{c^5}{G^3 M_\bullet^2 M_{\text{CO}}} a^4 (1 - e)^{7/2} \quad (3)$$

where we assumed that $M_{\text{CO}} \ll M_\bullet$. The dynamics of stellar objects can be described by delimiting two regions in the $(1 - e, a)$ plane (see Figure 2):

- (i) the region of stochastic evolution, where $t_{\text{rlx}} < t_{\text{GW}}$ and the orbital evolution is dominated by two-body encounters;
- (ii) the GW-dominated region, where $t_{\text{GW}} < t_{\text{rlx}}$, and the orbit evolution is dominated by the emission of GWs. Here the evolution is deterministic with increasingly good approximation as the CO's orbit shrinks.

Since relaxation for eccentric orbits changes $1 - e^2$ faster than a , objects in the region dominated by two-body relaxation will be slowly pushed, approximately at fixed a , to pericentres $r_p < r_{\text{cap}}$, resulting in gravitational captures. The value

$$r_{\text{cap}} = 8 GM_{\bullet}/c^2 = 3.8 \times 10^{-13} \text{ pc} \times (M_{\bullet}/M_{\odot}) \quad (4)$$

gives, for very eccentric orbits, the value of the angular momentum of the geodesics entering the horizon of the MBH (Merritt 2013). When including the emission of gravitational waves, it is possible to quantify the fraction of stellar objects entering r_{cap} directly (known as direct plunges), and those entering instead the GW-dominated region (thus forming an EMRI). With good approximation one can assume $r_{\text{LC}} = r_{\text{cap}}$, and count as direct plunges all the captures with semi-major axis larger than a critical value a_c , and count as EMRIs those with a smaller semi-major axis (Hopman & Alexander 2005; Bar-Or & Alexander 2016). This picture fails for $M_{\bullet} \lesssim 3 \times 10^5 M_{\odot}$, as EMRIs can form with a large semi-major axis due to abrupt emission of GWs at periastron (known as cliffhangers, see Qunbar & Stone 2024; Mancieri et al. 2025a). However, cliffhangers tend to be very eccentric and are unlikely to contribute significantly to the QPE population due to eccentricity constraints, as we will discuss later (Mancieri et al. 2025b). The critical semi-major axis can be estimated as the intersection between the line corresponding to $r_p = r_{\text{cap}}$ and the line $t_{\text{rlx}} = t_{\text{GW}}$ (cf. Fig. 2). We will consider nuclei such that $r_t > r_{\text{cap}}$, so that stellar EMRIs will be disrupted rather than being directly swallowed by the MBH.

2.2. QPE abundance

We estimate the number of active QPEs per galaxy at any instant t as $N_{\text{QPE}} = N_{\text{disk}} N_{\text{CO}}$ ³. To express N_{QPE} in terms of EMRI and TDE rates, we consider an observation starting at time t and lasting Δt_{obs} . During the observation time, we will see all the disks produced by disruptions that happened between $t - \tau_{\text{disk}}$ and $t + \Delta t_{\text{obs}}$. Similarly, the orbiter must be on an EMRI formed between $t - t_{\text{coal}}$ and $t + \Delta t_{\text{obs}}$ ⁴, where t_{coal} is the time required for the sBH to coalesce or, when considering stellar EMRIs, the time required for a star to reach its tidal disruption radius. Since EMRIs are formed along the curve $t_{\text{rlx}} = t_{\text{GW}}$ and have different coalescence times, for each type of orbiter we introduce the average coalescence time $\bar{t}_{\text{coal}} = N_{\text{EMRI}}^{\text{tot}}/\Gamma_{\text{EMRI}}$.

We assume that the EMRI rate Γ_{EMRI} and the TDE rate Γ_{TDE} do not change significantly over the timescales we are considering, so that $\dot{\Gamma}_{\text{TDE}} \tau_{\text{disk}} \ll \Gamma_{\text{TDE}}$ and $\dot{\Gamma}_{\text{EMRI}} t_{\text{coal}} \ll \Gamma_{\text{EMRI}}$. We also introduce the QPE selection factor $\mu^{T,e,i}$, that is the fraction of compact orbiters with T , e and i compatible with detectable QPEs:

$$\mu^{T,e,i} = \frac{N_{\text{CO}}}{N_{\text{EMRI}}^{\text{tot}}} \quad (5)$$

³ see Section 2

⁴ We avoid introducing here the time required for light to reach the observer, as it is a pure time shift. Moreover, for this computation we assume that compatible EMRIs will form a QPE immediately after they form. In fact, over these timescales the EMRI rate changes negligibly.

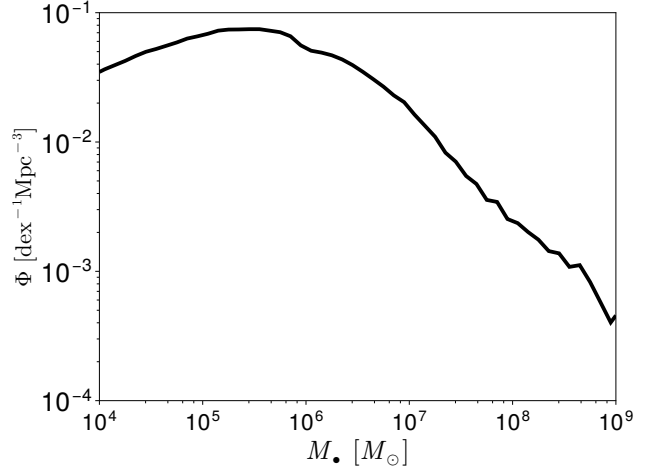


Fig. 3: Black Hole Mass Function Φ used in this work (from Izquierdo-Villalba et al. 2024).

The number of observed QPEs is:

$$\begin{aligned} N_{\text{QPE}}^{\text{obs}} &= N_{\text{disks}} N_{\text{CO}} \\ &= \int_{-\tau_{\text{disk}}}^{\Delta t_{\text{obs}}} dt' \Gamma_{\text{TDE}} \times \int_{-t_{\text{coal}}}^{\Delta t_{\text{obs}}} dt' \Gamma_{\text{CO}} \\ &\simeq \Gamma_{\text{TDE}} \Gamma_{\text{CO}} (\Delta t_{\text{obs}} + \tau_{\text{disk}}) (\Delta t_{\text{obs}} + t_{\text{coal}}) \\ &= \Gamma_{\text{TDE}} \tau_{\text{disk}} \Gamma_{\text{EMRI}} \mu^{T,e,i} \bar{t}_{\text{coal}} \\ &\quad + \Gamma_{\text{TDE}} \Gamma_{\text{EMRI}} \mu^{T,e,i} (\tau_{\text{disk}} + \bar{t}_{\text{coal}}) \Delta t_{\text{obs}} + O(\Delta t_{\text{obs}}^2). \quad (6) \end{aligned}$$

We recognize the first term as the number of QPEs that were active at time t , and the second as the formation rate of QPEs times the observation time Δt_{obs} . Therefore, in this work we estimate the QPE abundance per galaxy as

$$N_{\text{QPE}} = \Gamma_{\text{TDE}} \tau_{\text{disk}} \Gamma_{\text{EMRI}} \mu^{T,e,i} \bar{t}_{\text{coal}} \quad (7)$$

and the QPE formation rate per galaxy as

$$\Gamma_{\text{QPE}} = \Gamma_{\text{TDE}} \Gamma_{\text{EMRI}} \mu^{T,e,i} (\tau_{\text{disk}} + \bar{t}_{\text{coal}}) = N_{\text{QPE}} \left(\frac{1}{\tau_{\text{disk}}} + \frac{1}{\bar{t}_{\text{coal}}} \right). \quad (8)$$

The cosmic volumetric abundance of QPEs is computed by multiplying the per-galaxy abundance, $N_{\text{QPE}}(M_i, t)$ (Eq. (7)), by the local MBH mass function (that is, the number density of MBHs as a function of mass, see Figure 3) and integrating over M_{\bullet} . We caution that by doing so, we are implicitly assuming that TDE and EMRI rates are determined solely by the MBH mass, and that all MBHs are surrounded by an NSC, which have been shown to dominate the production of TDEs (Polkas et al. 2024).

In practice, we simulate 0.5dex equally log-spaced values of M_{\bullet} (cf. Sec. 3.1.1), and we compute the number density of QPEs n_{QPE}^i expected from MBHs in the i -th mass bin as:

$$n_{\text{QPE}}^i = N_{\text{QPE}}(M_i, t) \int_{\Delta M_i} d \log_{10}(M_{\bullet}) \Phi(M_{\bullet}), \quad (9)$$

where ΔM_i is a 0.5dex bin centered in the i -th value of the simulated MBH mass.

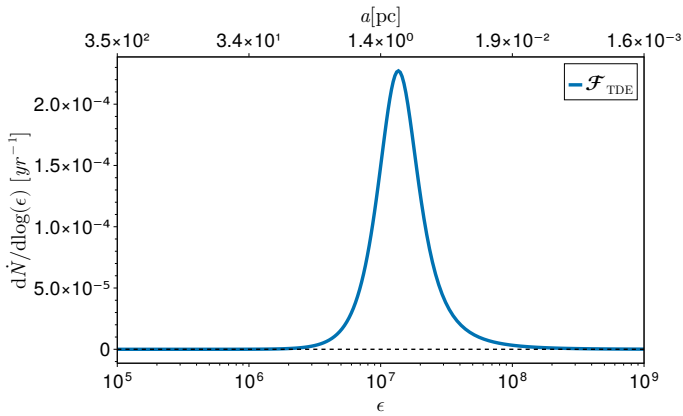


Fig. 4: Differential rate of TDEs, shown through the related function $d\dot{N}/d\log\epsilon = \epsilon\mathcal{F}_{\text{TDE}}$ as a function of the absolute value of the orbital energy $\epsilon = -E$ for a star with $M_{\text{CO}} = 1M_{\odot}$, $M_{\bullet} = 3 \times 10^6 M_{\odot}$, at $t = 8 \times 10^6 \text{yr}$. The peak of $d\dot{N}/d\log\epsilon$ is located at $r_c(E) = 0.884 \text{pc}$

Finally, to estimate the cosmic QPE volumetric abundance $\langle n_{\text{QPE}} \rangle$ for each bin, we average $n_{\text{QPE}}^i(t)$ over the simulation and sum over all bins of $\log_{10} M_{\bullet}$.⁵

$$\langle n_{\text{QPE}}^i \rangle = \frac{1}{t_{\text{end}} - t_0} \int_0^{t_{\text{end}}} dt n_{\text{QPE}}^i(t) \quad (10)$$

$$\langle n_{\text{QPE}} \rangle = \sum_i \langle n_{\text{QPE}}^i \rangle. \quad (11)$$

3. Simulations of two-body relaxation and loss cone rates

For each system, we compute the rate of TDEs and EMRIs, and estimate the fraction of compact orbiters compatible with the disk-impact model for QPEs, by evolving the distribution function of stars and BHs in the Fokker-Planck formalism.

3.1. PHASEFLOW runs

PHASEFLOW is a publicly available code, that simulates the two-body relaxation of spherical isotropic stellar systems (Vasiliev 2017). It solves the ergodic Fokker-Planck equation (Cohn 1980) and includes a sink term to account for loss cone captures. The one-dimensional approximation of relaxation in energy allows to span a wide range of parameters over very long evolution times, as the full 2D problem in energy and angular momentum is significantly more computationally expensive.

3.1.1. Initial conditions

We consider systems with $\log_{10} M_{\bullet}/M_{\odot} = \{5, 5.5, 6, 6.5, 7, 7.5, 8\}$. For each MBH mass, we model the surrounding NSC with three stellar populations: one of stars and two of sBHs. The stellar component has total mass $20M_{\bullet}$ and is composed of stars with mass $1M_{\odot}$. The sBHs components are formed by two populations of $10M_{\odot}$ and $40M_{\odot}$, respectively. Their abundance is chosen such that the $10M_{\odot}$ amount to a mass of $5/7 M_{\bullet}$, while those with $40M_{\odot}$ represent a mass of $2/7 M_{\bullet}$.⁶

⁵ $t + \Delta t_{\text{obs}} = t_{\text{end}}$

⁶ The proportions in total mass among the components match those obtained from the Kroupa Initial Mass Function (see Spera et al. 2016)

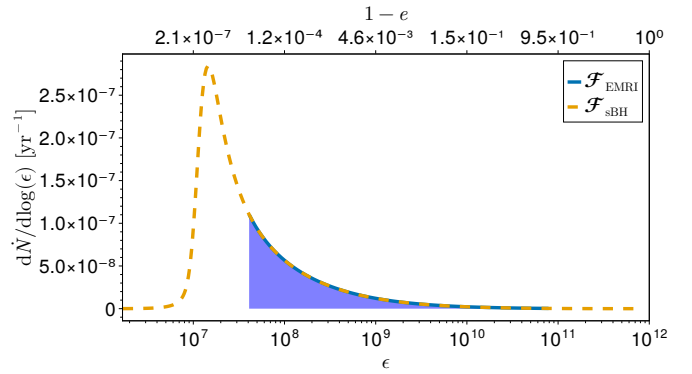


Fig. 5: Differential rate of EMRIs $\mathcal{F}_{\text{EMRI}}$ and direct plunges \mathcal{F}_{sBH} as functions of energy ϵ and eccentricity of the loss cone orbit e . We consider sBHs of $M_{\text{CO}} = 40M_{\odot}$ in a system with $M_{\bullet} = 3 \times 10^6 M_{\odot}$ that has relaxed for 1 Gyr. Our estimate of the EMRI rate is given by the light blue colour-filled area. The eccentricity at the peak of the differential rate is $1 - e = 3.35 \times 10^{-7}$.

As we anticipated, the capture radius of stars is, in the range of M_{\bullet} we consider, the *tidal radius* of Eq. (1). The capture radius for compact orbiters is the plunge radius Eq. (4) (see Subsection 2.1.2).

We set the size of the system so that the velocity dispersion σ of stars, at the corresponding influence radius $r_h = G M_{\bullet}/\sigma^2$, is on the $M_{\bullet} - \sigma$ relation (Ferrarese & Merritt 2000; Gebhardt et al. 2000). We compute σ according to the fit by Gültekin et al. (2009):

$$\sigma = 70 \text{ km/s} \times \left(\frac{M_{\bullet}}{1.53 \times 10^6 M_{\odot}} \right)^{1/4.24}. \quad (12)$$

We initialize each of the three components (stars, lighter sBHs, heavier sBHs) on a Dehnen profile with inner slope 1.5 (Dehnen 1993; Tremaine et al. 1994):

$$\rho = \rho_0 \left(\frac{r}{a} \right)^{-1.5} \left[1 + \left(\frac{r}{a} \right) \right]^{-2.5} \quad (13)$$

where ρ_0 is the density normalization; $a = 4 r_h$ is the *scale radius* ensuring the expected value of σ at the influence radius r_h .

The relaxation timescale of the system depends on its properties: in our case the larger the total mass, the slower the relaxation. We set for the cases with $M_{\bullet} \leq 3 \times 10^6 M_{\odot}$ a maximum timestep of 10^6yr , and for the others a maximum timestep of 10^7yr . In all cases the total time of integration is 10^{10}yr , as a proxy of the age of the Universe.

3.2. TDE rates

PHASEFLOW tracks in time the number of stars entering the capture radius with a given energy $\mathcal{F}_{\text{TDE}} = d\Gamma_{\text{TDE}}/dE$ (see Fig. 4). From this quantity, the TDE rates at time t can be computed as:

$$\Gamma_{\text{TDE}}(t) = \int_{-\infty}^0 dE \mathcal{F}_{\text{TDE}}(t, E). \quad (14)$$

and therefore

$$N_{\text{disks}}(t) = \Gamma_{\text{TDE}}(t) \tau_{\text{disk}}. \quad (15)$$

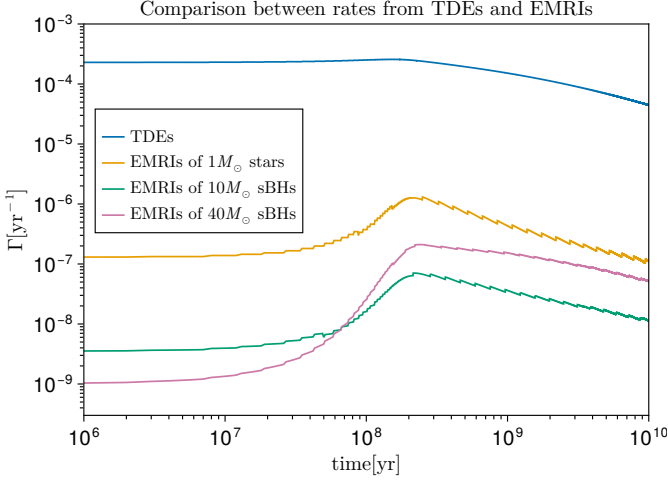


Fig. 6: Time dependent EMRI rates for stars of $1M_{\odot}$ (orange), sBH of $10M_{\odot}$ (green) and $40M_{\odot}$ (pink), and TDE rates (blue), for $M_{\bullet} = 3 \times 10^6 M_{\odot}$.

3.3. EMRI rates

In order to distinguish EMRIs from direct plunges, we compare the angular momentum relaxation timescale and the GW timescale of loss cone orbits⁷. Since it is used internally to compute the rate of disruptions, we recover the angular momentum relaxation time of loss cone orbits as computed by PHASEFLOW. Specifically, PHASEFLOW gives the diffusion coefficient \mathcal{D} , so that the relaxation time of an orbit is given by Eq. (2). The GW timescale is computed according to Eq. (3). Then, as presented in Subsection 2.1.2, we select EMRIs as objects captured on orbits such that $t_{\text{GW}} < t_{\text{rlx}}$.

Using the loss cone flux of a component $\mathcal{F}_{\text{CO}} = d\Gamma_{\text{CO}}/dE$ (see Fig. 5), we compute the rate of EMRI formation of that component as (see Fig. 6)

$$\Gamma_{\text{EMRI}}(t) = \int_{-\infty}^{E_{\text{GW}}} dE \mathcal{F}_{\text{CO}}(t, E) \quad (16)$$

where E_{GW} is the energy such that the curve $t_{\text{GW}} = t_{\text{rlx}}$ crosses the loss cone. The total number of EMRIs from that component must be computed by integrating over the $t_{\text{rlx}} = t_{\text{GW}}$ line as

$$N_{\text{EMRI}}^{\text{tot}} = \int dE \mathcal{F}_{\text{CO}}(t, E) t_{\text{coal}}(E) \quad (17)$$

where $t_{\text{coal}}(E)$ is the time-to-coalesce starting from the $t_{\text{rlx}} = t_{\text{GW}}$ curve with energy E .

4. Abundance and formation rate of QPEs

As we introduced in Sec. 2.2, we compute the number of disks N_{disk} around the MBH by multiplying the instantaneous $\Gamma_{\text{TDE}}(t)$ for τ_{disk} . The number of compact orbiters, on the other hand, depends on the details of the model—and crucially on its constraints on inclination and eccentricity at the QPE semi-major axis. EMRIs form with typical semi-major axes in the range of

⁷ For a semi-analytical approach to the 2D Fokker-Planck equation, see Kaur et al. (2024).

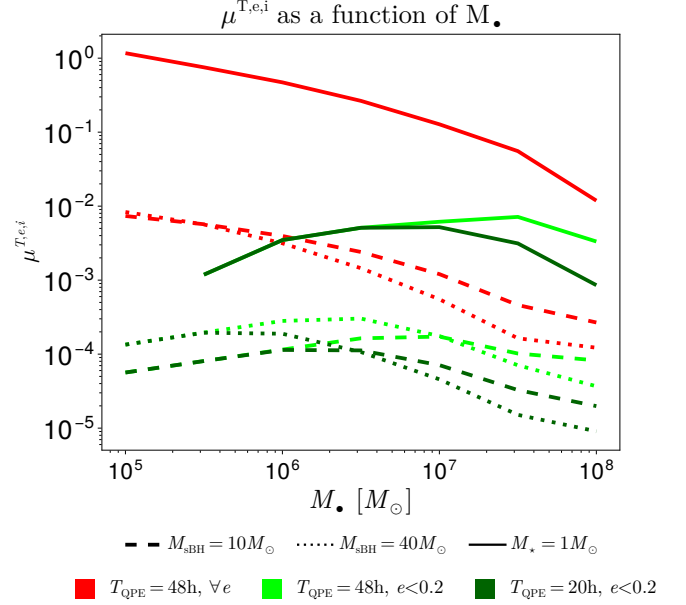


Fig. 7: QPE selection factor $\mu^{T,e,i} = N_{\text{CO}}/N_{\text{EMRI}}^{\text{tot}}$ as a function of M_{\bullet} , for different values of the maximum period T_{QPE} , and the maximum eccentricity $e_{\text{QPE}}^{\text{max}}$ compatible with QPEs.

$\sim 10^{-5} - 10^{-1}$ pc, with periods much longer than those of observed QPEs. Assuming the Keplerian estimate⁸

$$a_{\text{QPE}} \approx \sqrt[3]{GM_{\bullet} \left(\frac{T_{\text{QPE}}}{\pi} \right)^2} \quad (18)$$

we consider for reference⁹

$$a(48\text{h}) = 2.38 \times 10^{-7} \text{ pc} \times \left(\frac{M_{\bullet}}{M_{\odot}} \right)^{1/3}, \quad (19)$$

$$a(20\text{h}) = 1.34 \times 10^{-7} \text{ pc} \times \left(\frac{M_{\bullet}}{M_{\odot}} \right)^{1/3}, \quad (20)$$

$$a(9\text{h}) = 7.5 \times 10^{-8} \text{ pc} \times \left(\frac{M_{\bullet}}{M_{\odot}} \right)^{1/3}, \quad (21)$$

$$a(2\text{h}) = 2.9 \times 10^{-8} \text{ pc} \times \left(\frac{M_{\bullet}}{M_{\odot}} \right)^{1/3}. \quad (22)$$

4.1. Constraints on eccentricity and inclination

Once we fix the maximum a of observable QPEs $a_{\text{QPE}}^{\text{max}}$ and the maximum e compatible with the model $e_{\text{QPE}}^{\text{max}}$, we evolve the EMRIs formed on the $t_{\text{rlx}} = t_{\text{GW}}$ line up until their a and e are both within the constraints (cf. black dashed area in Figure 2). While $a_{\text{QPE}}^{\text{max}}$ can be constrained observationally from the typical recurrence timescales (through the period–semi-major-axis mapping),

⁸ We assume that the T_{QPE} is half the orbital period, as for every radial period the sBH typically pierces through the accretion disk twice.

⁹ We choose values corresponding to the recurrence period of AT2022upj (48 h) (Chakraborty et al. 2025), eRO-QPE3 (20 h) (Arcodia et al. 2024), GSN069 (9 h) (Miniutti et al. 2019) and eRO-QPE2 (2 h) (Arcodia et al. 2021).

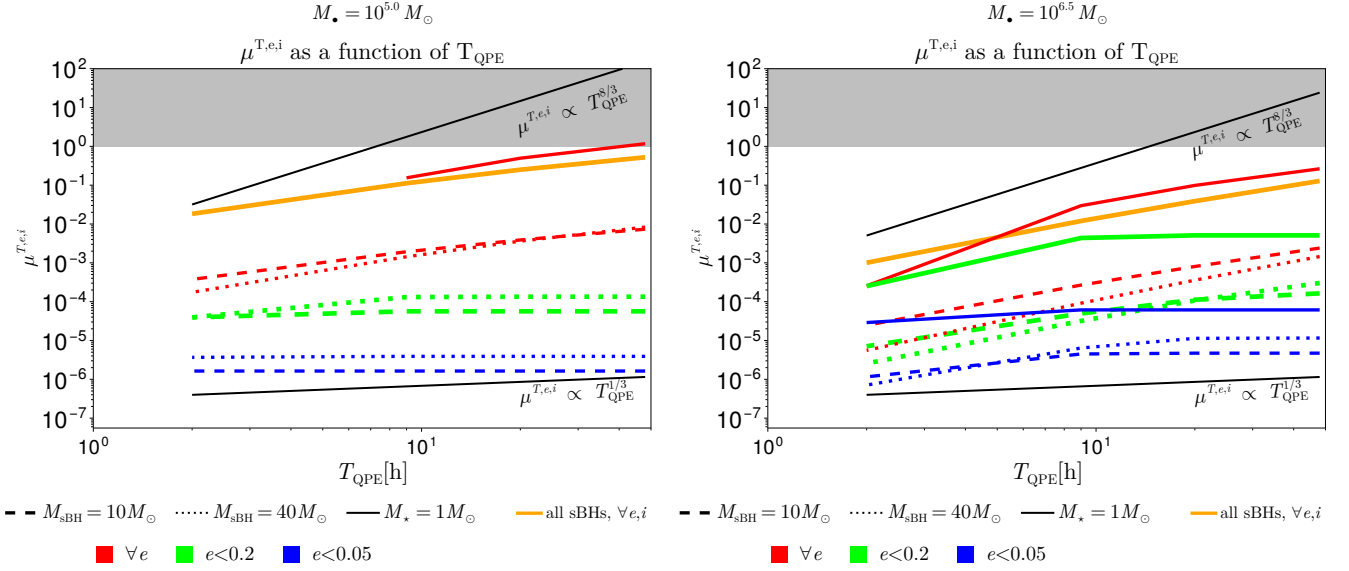


Fig. 8: QPE selection factor $\mu^{T,e,i} = N_{CO}/N_{EMRI}^{tot}$ for $M_* = 10^5 M_\odot$ (left) and $M_* = 3 \times 10^6 M_\odot$ (right), for different values of the maximum period T_{QPE} , and the maximum eccentricity e_{QPE}^{max} compatible with QPEs. The grey region marks parameter values for which μ would exceed unity; these are unphysical because μ is defined as a fraction of all EMRIs (hence $0 \leq \mu \leq 1$).

the same is not true for e_{QPE}^{max} . The relevant eccentricity threshold depends on the (still uncertain) physical mechanism responsible for QPE emission, and therefore we treat e_{QPE}^{max} as a model parameter.

We use the following strategy to compute the number of active QPEs from a snapshot of PHASEFLOW. For each energy bin along the $t_{rlx} = t_{GW}$ line, we consider its centre as the initial point of an EMRI trajectory (see Fig. 2 for a visual reference). From the 2.5 post-Newtonian orbit-averaged trajectory (Peters 1964) we find the eccentricity e_1 such that $a(e_1) = a_{QPE}^{max}$, where

$$a(e) = c_0 \frac{e^{12/19}}{1 - e^2} \left[1 + \frac{121}{304} e^2 \right]^{870/2299}. \quad (23)$$

where c_0 is determined by the initial condition of a and e . If $e_1 < e_{QPE}^{max}$, the trajectory is compatible with QPE orbiters from (e_1, a_{QPE}^{max}) to coalescence. If $e_1 > e_{QPE}^{max}$, we further evolve the trajectory up to $a_1 = a(e_{QPE}^{max})$; this trajectory is compatible with QPE orbiters from (e_{QPE}^{max}, a_1) until coalescence.

We show detailed examples of the possible evolution in phase space of $(1 - e, a)$ for two sBHs, as well as the selected $(1 - e, a)$ parameters of QPEs given $(1 - e_{QPE}^{max}, a_{QPE}^{max})$, in Fig. 2.

The process of two-body scattering is treated under the assumption of spherical symmetry. In a spherically symmetric potential around a non-spinning MBH, we expect the orbital angular-momentum directions of bound sBHs and stars to be isotropically distributed, i.e. with random orbital inclination i . This assumption may break down if MBH spin (Kerr geometry) and relativistic precession introduce a preference for prograde or low-inclination orbits, potentially modifying EMRI rates and the inclination distribution. Accordingly, the direction of angular momentum is set to be uniformly distributed on the sphere at the beginning of the GWs dominated phase. The probability that the relative i between the TDE disk and the EMRI orbit is smaller

than i_{QPE}^{max} is:

$$P(0 < i < i_{QPE}^{max}) = \frac{1}{2} \int_0^{i_{QPE}^{max}} d\theta \sin \theta \quad (24)$$

and for sBHs we choose a typical value $i_{QPE}^{max} = 20^\circ$, giving $P(i < i_{QPE}^{max}) = 0.03$. We set no constraints on the inclination of stellar EMRIs.

4.2. Coalescence time and N_{CO}

Considering that EMRI formed with energy E are compatible with QPEs only from (e_1, a_{QPE}^{max}) or (e_{QPE}^{max}, a_1) , to compute N_{CO} one must compute the coalescence time from that location. We estimate it as (Peters 1964)

$$t_{coal}^{QPE}(E) = \frac{12 c_0^4}{19 \beta} \times \int_{e_{fin}}^{e_{QPE}} \frac{de e^{29/19} [1 + (121/304)e^2]^{1181/2299}}{(1 - e^2)^{3/2}} \quad (25)$$

where c_0 is the quantity appearing in Eq. (23), while $e_{QPE} = e_1$ or e_{QPE}^{max} , and e_{fin} is the eccentricity at merger or disruption. Consequently, $r_{cap} = a(e_{fin})(1 - e_{fin})$ for sBHs, while for stars is the solution of $a(e_{fin})(1 - e_{fin}) = r_t$ using Eq. (23).

We can finally assemble the ingredients to compute the expected number of orbiters compatible with the QPE model

$$N_{CO}(t) = \int dE \mathcal{F}_{EMRI}(t, E) t_{coal}^{QPE}(E). \quad (26)$$

Then, using Eqs. (26) and (15), we compute the number of active QPEs as $N_{QPE} = N_{disks} N_{CO}$.

		M_{\bullet}																				
		$10^5 M_{\odot}$			$3 \times 10^5 M_{\odot}$			$10^6 M_{\odot}$			$3 \times 10^6 M_{\odot}$			$10^7 M_{\odot}$			$3 \times 10^7 M_{\odot}$			$10^8 M_{\odot}$		
		M_{CO}			M_{CO}			M_{CO}			M_{CO}			M_{CO}			M_{CO}			M_{CO}		
		$10 M_{\odot}$	$40 M_{\odot}$	$1 M_{\odot}$	$10 M_{\odot}$	$40 M_{\odot}$	$1 M_{\odot}$	$10 M_{\odot}$	$40 M_{\odot}$	$1 M_{\odot}$	$10 M_{\odot}$	$40 M_{\odot}$	$1 M_{\odot}$	$10 M_{\odot}$	$40 M_{\odot}$	$1 M_{\odot}$	$10 M_{\odot}$	$40 M_{\odot}$	$1 M_{\odot}$	$10 M_{\odot}$	$40 M_{\odot}$	$1 M_{\odot}$
T_{QPE}	$e_{\text{QPE}}^{\text{max}}$																					
48 h	0.05	1.6×10^{-6}	3.9×10^{-6}	0.0	2.3×10^{-6}	5.7×10^{-6}	0.0	3.3×10^{-6}	8.2×10^{-6}	3.1×10^{-6}	4.8×10^{-6}	1.2×10^{-5}	6.1×10^{-5}	6.7×10^{-6}	1.6×10^{-5}	1.4×10^{-4}	8.8×10^{-6}	1.4×10^{-5}	2.52×10^{-4}	1.3×10^{-5}	6.4×10^{-6}	4.4×10^{-4}
	0.2	5.6×10^{-5}	1.3×10^{-4}	0.0	8.1×10^{-5}	2.0×10^{-4}	0.0012	1.1×10^{-4}	2.8×10^{-4}	0.0035	1.6×10^{-4}	3.0×10^{-4}	0.0051	1.7×10^{-4}	1.8×10^{-4}	0.0061	1.0×10^{-4}	7.1×10^{-5}	0.0073	7.7×10^{-5}	3.6×10^{-5}	0.0036
	1	0.0074	0.0083	1.0	0.0057	0.0056	0.75	0.0040	0.0031	0.47	0.0024	0.0014	0.26	0.0012	5.5×10^{-4}	0.13	4.6×10^{-4}	1.6×10^{-4}	0.056	3.2×10^{-4}	1.5×10^{-4}	0.013
20 h	0.05	1.6×10^{-6}	3.9×10^{-6}	0.0	2.3×10^{-6}	5.7×10^{-6}	0.0	3.3×10^{-6}	8.2×10^{-6}	3.1×10^{-6}	4.8×10^{-6}	1.1×10^{-5}	6.1×10^{-5}	6.5×10^{-6}	9.5×10^{-6}	1.4×10^{-4}	5.0×10^{-6}	4.4×10^{-6}	2.47×10^{-4}	4.3×10^{-6}	2.0×10^{-6}	1.9×10^{-4}
	0.2	5.6×10^{-5}	1.3×10^{-4}	0.0	8.1×10^{-5}	1.9×10^{-4}	0.0012	1.1×10^{-4}	1.9×10^{-4}	0.0035	1.1×10^{-4}	1.1×10^{-4}	0.0051	7.1×10^{-5}	4.6×10^{-5}	0.0052	3.4×10^{-5}	1.5×10^{-5}	0.0032	2.3×10^{-5}	1.1×10^{-5}	0.0011
	1	0.0039	0.0036	0.49	0.0026	0.0020	0.34	0.0015	9.2×10^{-4}	0.20	8.1×10^{-4}	3.6×10^{-4}	0.099	3.5×10^{-4}	1.2×10^{-4}	0.041	1.1×10^{-4}	2.9×10^{-5}	0.015	7.4×10^{-5}	3.3×10^{-5}	0.0025
9 h	0.05	1.6×10^{-6}	3.9×10^{-6}	0.0	2.3×10^{-6}	5.7×10^{-6}	0.0	3.3×10^{-6}	7.9×10^{-6}	3.1×10^{-6}	4.5×10^{-6}	6.4×10^{-6}	6.1×10^{-5}	3.8×10^{-6}	3.2×10^{-6}	1.4×10^{-4}	2.0×10^{-6}	1.2×10^{-6}	1.5×10^{-4}	-	-	-
	0.2	5.6×10^{-5}	1.3×10^{-4}	0.0	7.9×10^{-5}	1.3×10^{-4}	0.0012	7.6×10^{-5}	7.2×10^{-5}	0.0035	5.0×10^{-5}	3.2×10^{-5}	0.0044	2.6×10^{-5}	1.2×10^{-5}	0.0025	1.1×10^{-5}	3.3×10^{-6}	0.0012	-	-	-
	1	0.0019	0.0014	0.15	0.0011	6.7×10^{-4}	0.12	5.8×10^{-4}	2.6×10^{-4}	0.067	2.7×10^{-4}	9.2×10^{-5}	0.030	9.9×10^{-5}	2.6×10^{-5}	0.011	2.5×10^{-6}	5.2×10^{-6}	0.0038	-	-	-
2 h	0.05	1.6×10^{-6}	3.7×10^{-6}	0.0	2.2×10^{-6}	3.2×10^{-6}	0.0	1.9×10^{-6}	1.7×10^{-6}	3.1×10^{-6}	1.2×10^{-6}	7.2×10^{-7}	2.9×10^{-5}	6.2×10^{-7}	2.6×10^{-7}	2.1×10^{-5}	-	-	-	-	-	-
	0.2	3.9×10^{-5}	3.9×10^{-5}	0.0	2.7×10^{-5}	1.9×10^{-5}	3.5×10^{-4}	1.5×10^{-5}	7.3×10^{-6}	4.4×10^{-4}	7.4×10^{-6}	2.6×10^{-6}	2.5×10^{-4}	3.0×10^{-6}	7.3×10^{-7}	1.0×10^{-4}	-	-	-	-	-	-
	1	3.7×10^{-4}	1.7×10^{-4}	0.0	1.8×10^{-4}	6.4×10^{-4}	3.8×10^{-4}	7.4×10^{-5}	2.1×10^{-5}	4.5×10^{-4}	2.6×10^{-5}	5.7×10^{-6}	2.6×10^{-4}	6.0×10^{-6}	1.1×10^{-6}	1.0×10^{-4}	-	-	-	-	-	-

Table 1: QPE selection factor $\mu^{T,e,i} = N_{\text{CO}}/N_{\text{EMRI}}^{\text{tot}}$ for different values of the maximum period T_{QPE} , and the maximum eccentricity $e_{\text{QPE}}^{\text{max}}$ compatible with QPEs. We consider NSCs with central MBH of mass M_{\bullet} and EMRIs from COs of different mass M_{CO} . For sBHs ($M_{\text{CO}} = 10, 40 M_{\odot}$) $\mu^{T,e,i}$ also accounts for inclination constraints $0^{\circ} < i < 20^{\circ}$. “-” means that the period at r_{cap} is longer than T_{QPE} .

		M_{\bullet}																				
		$10^5 M_{\odot}$			$3 \times 10^5 M_{\odot}$			$10^6 M_{\odot}$			$3 \times 10^6 M_{\odot}$			$10^7 M_{\odot}$			$3 \times 10^7 M_{\odot}$			$10^8 M_{\odot}$		
		M_{CO}			M_{CO}			M_{CO}			M_{CO}			M_{CO}			M_{CO}			M_{CO}		
		$10 M_{\odot}$	$40 M_{\odot}$	$1 M_{\odot}$	$10 M_{\odot}$	$40 M_{\odot}$	$1 M_{\odot}$	$10 M_{\odot}$	$40 M_{\odot}$	$1 M_{\odot}$	$10 M_{\odot}$	$40 M_{\odot}$	$1 M_{\odot}$	$10 M_{\odot}$	$40 M_{\odot}$	$1 M_{\odot}$	$10 M_{\odot}$	$40 M_{\odot}$	$1 M_{\odot}$	$10 M_{\odot}$	$40 M_{\odot}$	$1 M_{\odot}$
T_{QPE}	$e_{\text{QPE}}^{\text{max}}$																					
48 h	0.05	5.0×10^{-14}	10^{-12}	0.0	6.0×10^{-13}	1.2×10^{-11}	0.0	6.6×10^{-12}	1.3×10^{-10}	1.1×10^{-11}	6.6×10^{-11}	1.2×10^{-9}	10^{-6}	8.6×10^{-10}	1.4×10^{-8}	4.2×10^{-7}	4.3×10^{-9}	3.4×10^{-8}	3.7×10^{-6}	6.7×10^{-10}	2.3×10^{-10}	7.4×10^{-6}
	0.2	1.7×10^{-12}	3.5×10^{-11}	0.0	2.1×10^{-11}	4.2×10^{-10}	1.8×10^{-10}	2.3×10^{-10}	4.5×10^{-9}	3.6×10^{-8}	2.3×10^{-9}	3.5×10^{-8}	10^{-6}	2.2×10^{-8}	1.6×10^{-7}	1.8×10^{-5}	5.0×10^{-8}	1.7×10^{-7}	10^{-4}	4.0×10^{-9}	1.3×10^{-9}	6.0×10^{-5}
	1	2.8×10^{-10}	2.9×10^{-9}	3.5×10^{-9}	1.9×10^{-9}	1.6×10^{-8}	4.0×10^{-7}	9.5×10^{-9}	6.5×10^{-8}	7.4×10^{-6}	3.8×10^{-8}	1.8×10^{-7}	6.1×10^{-5}	1.5×10^{-7}	4.9×10^{-7}	3.8×10^{-4}	2.2×10^{-7}	3.4×10^{-7}	8.2×10^{-4}	1.6×10^{-8}	5.4×10^{-9}	2.2×10^{-4}
20 h	0.05	5.0×10^{-14}	10^{-12}	0.0	6.0×10^{-13}	1.2×10^{-11}	0.0	6.6×10^{-12}	1.3×10^{-10}	1.1×10^{-11}	6.6×10^{-11}	1.2×10^{-10}	9.9×10^{-9}	8.2×10^{-10}	8.4×10^{-9}	4.2×10^{-7}	2.4×10^{-9}	1.1×10^{-8}	3.6×10^{-6}	2.2×10^{-10}	7.3×10^{-11}	3.1×10^{-6}
	0.2	1.7×10^{-12}	3.5×10^{-11}	0.0	2.1×10^{-11}	4.2×10^{-10}	1.8×10^{-10}	2.2×10^{-10}	3.5×10^{-9}	3.6×10^{-8}	1.7×10^{-9}	1.3×10^{-8}	10^{-6}	9.1×10^{-9}	4.1×10^{-8}	1.6×10^{-5}	1.6×10^{-8}	3.7×10^{-8}	4.7×10^{-5}	1.2×10^{-9}	4.0×10^{-10}	1.9×10^{-5}
	1	1.6×10^{-10}	1.3×10^{-9}	1.3×10^{-9}	9.0×10^{-10}	6.2×10^{-9}	1.8×10^{-7}	3.9×10^{-9}	1.9×10^{-8}	3.2×10^{-6}	1.3×10^{-8}	4.5×10^{-8}	2.3×10^{-5}	4.4×10^{-8}	1.0×10^{-7}	1.2×10^{-4}	5.3×10^{-8}	7.0×10^{-8}	2.2×10^{-4}	3.8×10^{-9}	1.2×10^{-9}	4.3×10^{-5}
9 h	0.05	5.0×10^{-14}	10^{-12}	0.0	6.0×10^{-13}	1.2×10^{-11}	0.0	6.6×10^{-12}	1.3×10^{-10}	1.1×10^{-11}	6.4×10^{-11}	7.7×10^{-10}	9.9×10^{-9}	4.8×10^{-10}	2.8×10^{-9}	4.2×10^{-7}	9.8×10^{-10}	2.9×10^{-9}	2.1×10^{-6}	-	-	-
	0.2	1.7×10^{-12}	3.5×10^{-11}	0.0	2.1×10^{-11}	3.4×10^{-10}	1.8×10^{-10}	1.8×10^{-10}	1.5×10^{-9}	3.6×10^{-8}	7.9×10^{-10}	4.0×10^{-9}	9.4×10^{-7}	3.3×10^{-9}	10^{-8}	7.5×10^{-6}	5.2×10^{-9}	8.1×10^{-9}	1.8×10^{-5}	-	-	-
	1	8.2×10^{-11}	5.6×10^{-10}	3.4×10^{-10}	4.1×10^{-10}	2.1×10^{-9}	6.1×10^{-8}	1.5×10^{-9}	5.7×10^{-9}	1.1×10^{-6}	4.3×10^{-9}	1.1×10^{-8}	7.1×10^{-6}	1.2×10^{-8}	2.3×10^{-8}	3.4×10^{-5}	1.2×10^{-8}	1.3×10^{-8}	5.5×10^{-5}	-	-	-
2 h	0.05	5.0×10^{-14}	10^{-12}	0.0	6.0×10^{-13}	9.0×10^{-12}	0.0	4.6×10^{-12}	3.6×10^{-11}	1.1×10^{-11}	1.9×10^{-11}	9.1×10^{-11}	5.6×10^{-9}	7.9×10^{-11}	2.3×10^{-10}	6.3×10^{-8}	-	-	-	-	-	-
	0.2	1.5×10^{-12}	1.5×10^{-11}	0.0	9.6×10^{-12}	6.0×10^{-11}	6.1×10^{-11}	3.8×10^{-11}	1.6×10^{-10}	6.2×10^{-9}	1.2×10^{-10}	3.2×10^{-10}	6.0×10^{-8}	3.9×10^{-10}	6.5×10^{-10}	3.1×10^{-7}	-	-	-	-	-	-
	1	1.7×10^{-11}	7.3×10^{-11}	0.0	6.6×10^{-11}	2.1×10^{-10}	6.8×10^{-11}	1.9×10^{-10}	4.5×10^{-10}	6.4×10^{-9}	4.0×10^{-10}	6.8×10^{-10}	6.1×10^{-8}	7.6×10^{-10}	9.6×10^{-10}	3.1×10^{-7}	-	-	-	-	-	-

Table 2: Average number of active QPEs $\langle N_{\text{QPE}} \rangle$ over 10 Gyr, as estimated from two-body relaxation simulations. We use the same symbols as in Table 1. At each snapshot of the simulation, we compute $N_{\text{QPE}} = N_{\text{disks}} N_{\text{CO}}$ as explained in Sec. 4. “-” means that the period at r_{cap} is longer than T_{QPE} .

5. Results

We summarize in this section the results of our analysis on the number of QPEs in the NSCs we consider, and on the inferred cosmic abundance of QPEs.

In Table 1 we present the average QPE selection factor $\mu^{T,e,i}$, which is the fraction of EMRIs compatible with QPEs over 10 Gyrs of simulation. We remark that it is defined in terms of three parameters: the maximum inclination $i_{\text{QPE}}^{\text{max}}$, the maximum eccentricity $e_{\text{QPE}}^{\text{max}}$, and the maximum orbital period T_{QPE} . Even if the disk-impact model does not impose direct constraints on the eccentricity of stellar orbiters, the impact of $e_{\text{QPE}}^{\text{max}}$ is non-trivial, so we include it for the sake of completeness. We set $i_{\text{QPE}}^{\text{max}} = 20^\circ$ for sBHs and no constraints on i for stars. The scalings of \dot{a} and \dot{e} impact directly the trend of $\mu^{T,e,i}$ because of GW emission. At fixed constraints on e and T , the fraction of COs compatible with QPEs decreases when M_\bullet increases for large M_\bullet , as T_{QPE} restricts to a smaller and smaller fraction of EMRIs. At small M_\bullet the circularization due to GW emission can reduce $\mu^{T,e,i}$, especially in the case of sBHs (see Fig. 7). The number of objects with semi-major axis smaller than a behaves like t_{GW} (e.g. Amaro-Seoane et al. 2017), setting the scaling of $\mu^{T,e,i}$ for $e_{\text{QPE}}^{\text{max}} = 1$. As $t_{\text{GW}} \sim a^{1/2} \sim T^{1/3}$ for very eccentric orbits and $t_{\text{GW}} \sim a^4 \sim T^{8/3}$ for nearly circular orbits, the scalings we find are bound by these two extremes. Due to the mixed eccentricity distribution, $\mu^{T,e,i}$ is almost linear with T_{QPE} at $M_\bullet = 10^5 M_\odot$, while for larger M_\bullet it becomes steeper (see Fig. 8). In general, most EMRIs are found at moderate eccentricities, so that the impact of the eccentricity cut is evident for both sBHs and stars: larger $e_{\text{max}}^{\text{QPE}}$ gives larger $\mu^{T,e,i}$, although the magnitude of the change depends on the mass of the stellar object and the NSC. $\mu^{T,e,i}$ is generally comparable among the two species of sBHs, but is typically larger for stars because there is no inclination constraint and they are lighter. In fact, the GW dominated region for stars is smaller, and a larger fraction corresponds to periods compatible with QPEs. However, for large M_\bullet the period at r_t is so long that $\mu^{T,e,i} = 0$ for the shortest values of T_{QPE} . For SMBH masses of $3 \times 10^7 M_\odot$ and $10^8 M_\odot$, the same happens when the period at r_{cap} is longer than T_{QPE} (see Table 1).

In Figs. 9 and 10 we show the number of active QPEs N_{QPE} for two representative systems in time. Since it can be expressed in terms of the abundance (Eq. (8)), assuming $\tau_{\text{disk}} \ll \bar{t}_{\text{coal}}$, the formation rate is $\Gamma_{\text{QPE}} = N_{\text{QPE}}/\tau_{\text{disk}}$, and the two quantities follow the same trend. At $t \gtrsim 1$ Gyr, N_{QPE} starts to decline, following the long term evolution of loss cone event rates. We report in Table 2 the time average value $\langle N_{\text{QPE}} \rangle$ over 10 Gyr for all the NSCs we consider. Since $N_{\text{EMRI}}^{\text{tot}}$ depends weakly on the mass of the orbiter at fixed M_\bullet , $\langle N_{\text{QPE}} \rangle$ follows the same qualitative trends as $\mu^{T,e,i}$. Similarly, the scaling of loss cone rates with M_\bullet mildly affects that of $\mu^{T,e,i}$.

Finally, we combine our results with the MBH mass function to compute the cosmic QPE abundance $\langle n_{\text{QPE}} \rangle$, as described in Subsection 2.2. In Fig. 11 we present $\langle n_{\text{QPE}} \rangle$ for $T_{\text{QPE}} = \{2, 9, 20, 48\}$ h and $e_{\text{QPE}}^{\text{max}} = \{0.05, 0.2, 1\}$ ¹⁰. Considering $T_{\text{QPE}} \gtrsim 9$ h, rates can vary by 2 – 3 orders of magnitude depending on the adopted eccentricity constraints, and within an order of magnitude depending on the period constraints. Overall, stellar QPEs are $\sim 10^3$ more numerous than sBHs QPEs at fixed constraints.

Arcodia et al. (2024) estimate a cosmic QPE abundance of $(1.7 \times 10^{-7} - 5 \times 10^{-6}) \text{ Mpc}^{-3}$, which is compatible with our estimates for QPEs in the disk-impact model from stellar EMRIs. By removing eccentricity and inclination constraints, sBHs QPEs are compatible with the lower end of such estimates. See the next section for a more detailed discussion.

6. Discussion

We will now discuss the assumptions and the limitations of our results.

6.1. EMRI formation channels

Our model focuses on the classical EMRI formation channel, but various alternative dynamical channels have been proposed. Among those, some might have cosmological rates comparable to or larger than spherical two-body relaxation, especially when restricting to small eccentricities and sBHs. For example, a member of a stellar binary might be deposited as the result of a three-body encounter with the central MBH (Binary deposition Miller et al. 2005). Such a channel might favour small eccentricity with comparable rates (Raveh & Perets 2021). If the central MBH is surrounded by a disk, it can capture compact objects because of inclination damping, and further reduce the orbital eccentricity as the compact object migrates towards the MBH (e.g. Syer et al. 1991; Šubr & Karas 1999; Karas & Šubr 2001; Levin 2007; Kocsis et al. 2011). This channel seems to be very promising for producing EMRIs¹¹ with small eccentricity (Sun et al. 2025). Alternatively, a star or an sBH might form in the disk (e.g. Artymowicz et al. 1993; Levin 2003; Goodman & Tan 2004), or multiple mergers can increase the size of sBHs. Since EMRI formation rates in these scenarios suffer of very large uncertainties, we do not venture into computing the corresponding expected QPE rates; however, the current formalism can be readily applied to any EMRI formation channel.

6.2. Dynamics in the NSC

As we explained in Sec. 2, the effects of GW emission are not included in 1D Fokker-Planck models as PHASEFLOW, primarily for the significant impact of eccentricity. We neglect the spin of the primary MBH, that might increase the number of EMRIs and affect the inclination distribution (e.g. Zhang & Amaro Seoane 2025; Sun et al. 2025). Deviations from spherical symmetry might increase loss cone rates (most importantly the TDE rate), even though the impact might be minor for the small MBHs we consider (Vasiliev & Merritt 2013). Similarly, a steep gaseous profile might affect the evolution of objects because of significant dynamical friction (Rozner & Ramirez-Ruiz 2025).

Currently, loss cone theory neglects partial tidal disruptions and Roche lobe overflows of the star, accounting solely for the possibility of complete tidal disruption (Cohn & Kulsrud 1978; Merritt 2013; Broggi 2025). The TDE rate might be marginally affected for small M_\bullet (e.g., Bortolas et al. 2023; Broggi et al. 2024). However, as EMRIs require repeated passages at small pericentre, these effects might significantly impact the rate of stellar EMRIs and, consequently, the related QPE abundance.

¹¹ see Pan & Yang (2021)

¹⁰ Physically, the maximum possible eccentricity is set by the minimum pericentre r_{cap} or r_t .

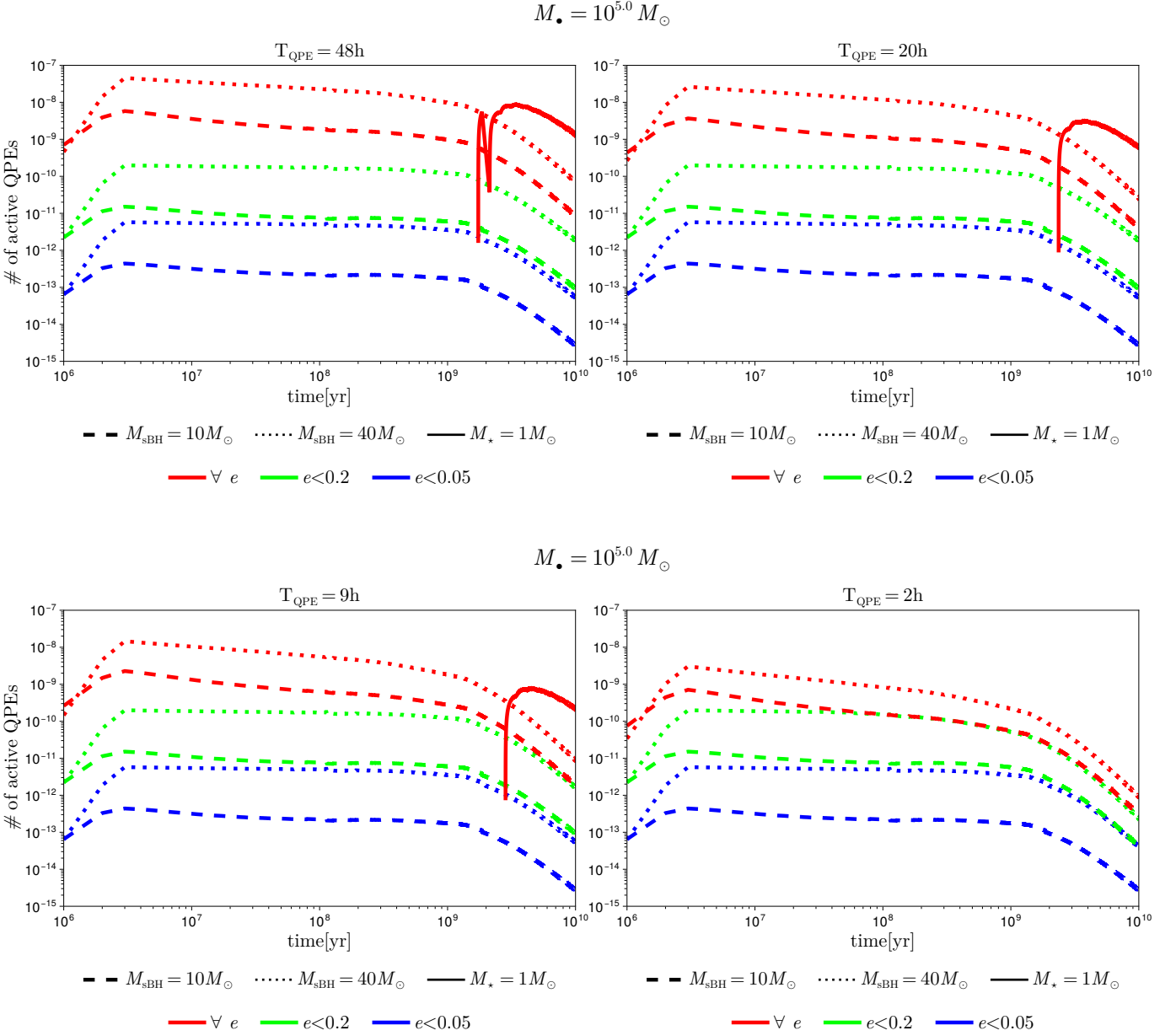


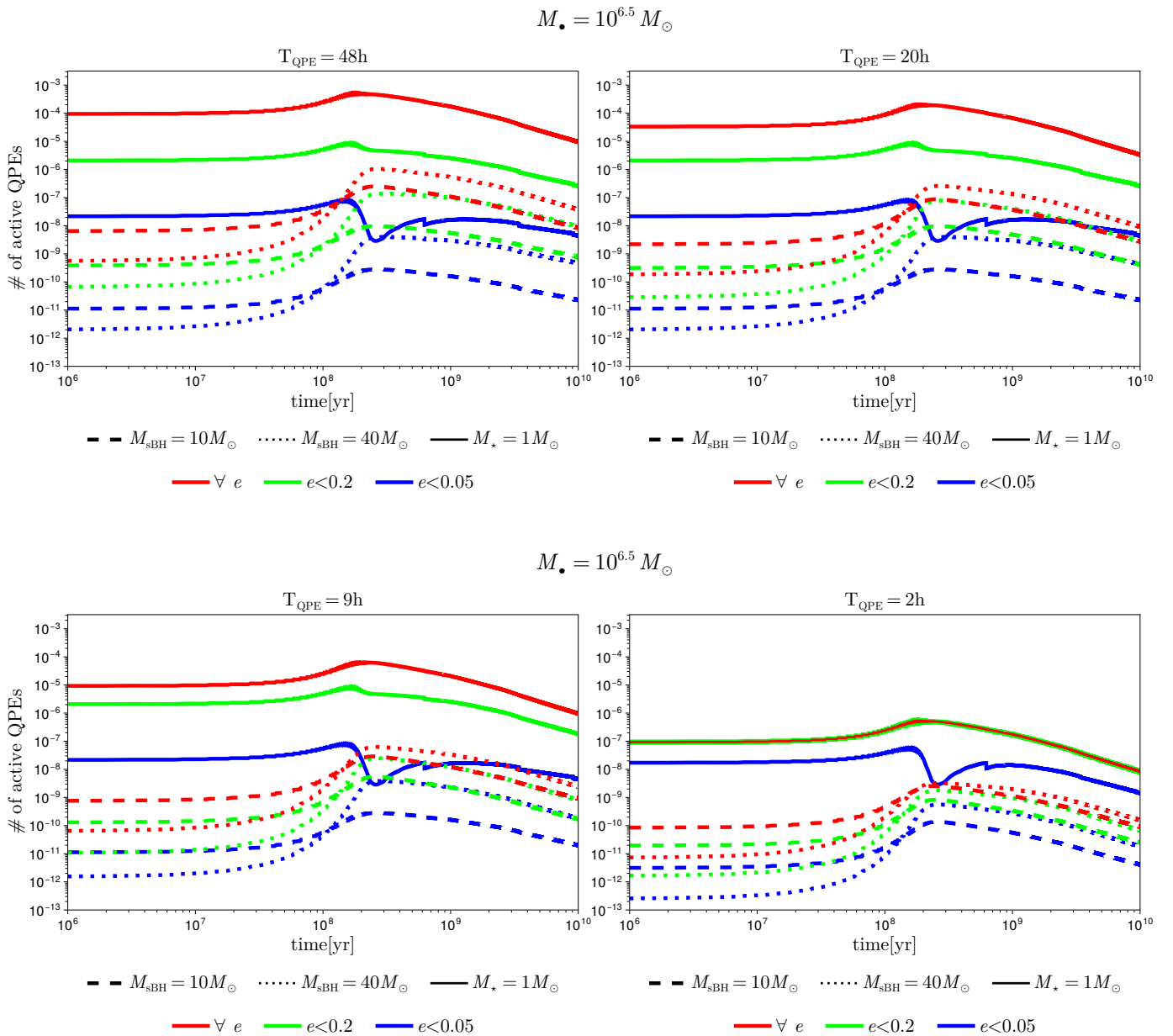
Fig. 9: Number of active QPEs of sBHs of $10M_{\odot}$ (dashed line), $40M_{\odot}$ (dotted line), and stars of $1M_{\odot}$ (solid line) around a MBH of $10^5 M_{\odot}$. Different colors are for different limiting eccentricities, as marked in the figure. The four panels are for different values of T_{QPE} (on the first row: $T_{\text{QPE}}=48\text{h}$ on the left, 20h on the right, on the second row: $T_{\text{QPE}}=9\text{h}$ on the left, 2h on the right).

6.3. Galactic population

We assume that every MBH is surrounded by a NSC with properties fixed by its mass. Naturally, not all MBHs have a NSC. Moreover, the properties of NSCs vary systematically with host galaxy mass and morphology (Neumayer et al. 2020), suggesting that the initial phase of the relaxation process and the total available mass budget in our simple NSC model might be inadequate. At later stage, relaxation dictates the stellar profile, possibly reducing the uncertainty when considering the cosmic population. Finally, we model the stellar distribution using only three mass components. This approximation simplifies the impact of mass segregation on the mass spectrum, which might play an important role and modify loss-cone rates time-dependently (Bortolas 2022).

6.4. Observability of QPEs

We do not include observability constraints on disk/EMRI systems. However, emission mechanisms with a preferential axis or the properties of the TDE disk might reduce the number of observable systems. In fact, electromagnetic emission in the disk-impact model is not fully understood. The bubble generated as the object crosses the disk cools until it becomes optically thin; at that stage, its temperature settles to the inferred temperature T_{obs} , crucially set by the cooling process. These open points directly impact our rates through orbital constraints. For example, very eccentric EMRIs from sBHs might reach pericenters so small that the density of the disk is considerable; despite the small Bondi radius, the passage might strip as much mass as in

Fig. 10: Same as Fig. 9 but for a central MBH of $3 \times 10^6 M_{\odot}$

the circular case, producing a comparably luminous flare, thus relaxing eccentricity constraints.

6.5. Constraints from timing models

The first results from fitting the timing of QPEs with dynamical models (see e.g. Zhou et al. 2024) indicate a preference for small eccentricity, with no assumptions on the type of orbiter. While this might be caused by the size of Bondi radius for sBHs, stellar QPEs from standard two-body relaxation should favour large eccentricity. Restricting the maximum eccentricity affects expectations on the number density of QPEs by orders of magnitude, possibly pushing it outside of currently inferred values.

7. Conclusions

We built a framework to compute the number of expected QPEs produced by two-body relaxation in the disk-impact model. We assume a Schwarzschild MBH and a spherically symmetric potential.

We linked the QPE volumetric abundance to the formation rate of EMRIs and TDEs, which we modeled by simulating the relaxation of NSCs around MBHs of mass $M_{\bullet} = 10^5 - 10^8 M_{\odot}$ using the Fokker-Planck integration code PHASEFLOW (Vasiliev 2017).

Each NSC was modeled with three mass components: main sequence stars of $1 M_{\odot}$, and two families of sBHs with masses of $10 M_{\odot}$ and $40 M_{\odot}$. We evolved the systems for 10 Gyr, tracking the evolution of the TDE and EMRI rates. Finally, we selected EMRI events within the constraints arising from the emission model: the maximum orbital period T_{QPE} , and for sBHs the

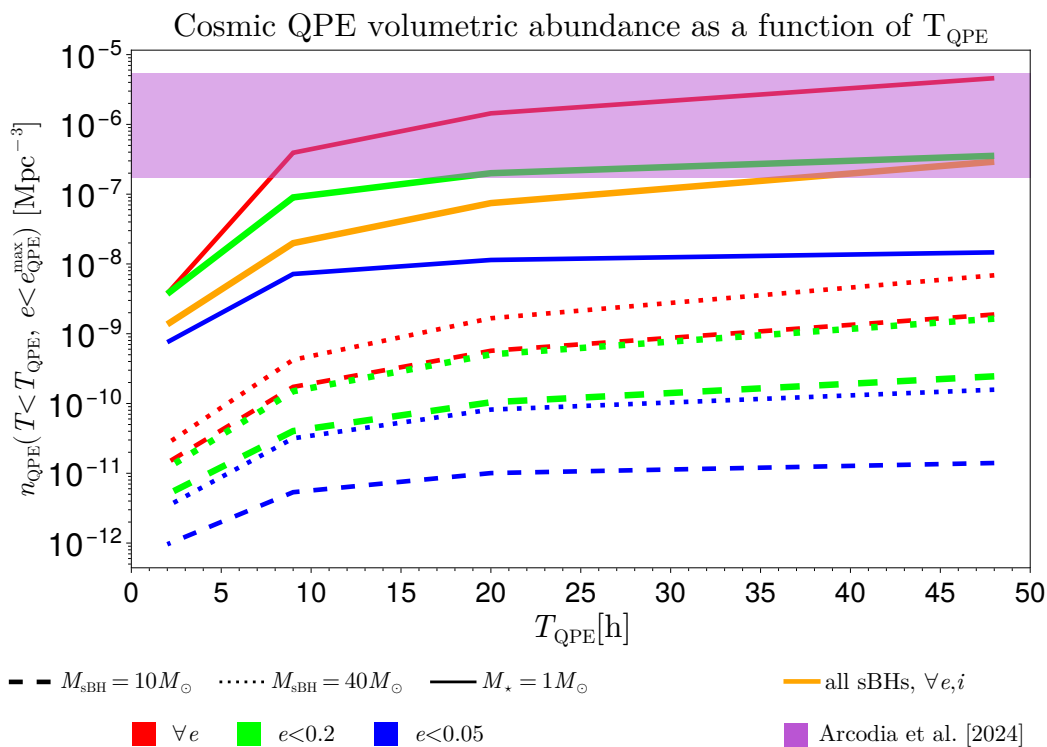


Fig. 11: Cosmic volumetric abundance assuming a limiting eccentricity of 0.05, 0.2, 1.0 for sBHs of $10M_{\odot}$ (dashed line) and $40M_{\odot}$ (dotted line). The cosmic volumetric abundance of stars (solid line) is portrayed at $e=0.05, 0.2, 1-r_1/a_{\text{QPE}}$. The orange solid line corresponds to the sum of the n_{QPE} of both sBHs without accounting for the constraints on e and i . The violet band corresponds to the QPE volumetric abundance found by Arcodia et al. (2024).

maximum eccentricity $e_{\text{QPE}}^{\text{max}} \approx 0.2$ and the maximum inclination $0 < i < i_{\text{QPE}}^{\text{max}} \approx 20^{\circ}$. By assuming that all MBHs are surrounded by an NSC, we combined our results with the BH mass function to estimate the QPE abundance in the universe.

We found that the QPE volumetric abundance (or number density) can vary in the range 10^{-12}Mpc^{-3} to 10^{-6}Mpc^{-3} depending on the imposed constraints (see Fig. 11). QPEs powered by impacting stars can be as frequent as suggested by first observational estimates (Arcodia et al. 2024). Conversely, the constraints on the orbital properties of sBHs significantly reduce the number of observable QPEs, which are $\sim 10^3$ times less numerous than stellar ones and generally below observational estimates.

Removing inclination and eccentricity constraints, QPEs from sBHs are compatible to the lower end of observational predictions for $T_{\text{QPE}} = 48\text{h}$. In general, two-body relaxation induces a preference for eccentric sources, in contrast with the picture emerging from fitting of QPE timing. Restricting to low-eccentricity sources significantly reduces the rate, possibly to values incompatible with observational estimates both for stars and sBHs.

By including other formation channels for EMRIs, a more detailed dynamical model and more refined galactic models, it might be possible to probe, constrain and rule-out dynamical models of QPEs. Shedding light on their nature and understanding their possible connection to EMRIs might unveil them as an electromagnetic counterpart of future LISA sources, opening new avenues in multimessenger astronomy.

Acknowledgements. AS acknowledges financial support provided under the European Union’s H2020 ERC Advanced Grant “PINGU” (Grant Agreement: 101142079). MB acknowledges support from the Italian Ministry for Universities and Research (MUR) program “Dipartimenti di Eccellenza 2023-2027”, within the framework of the activities of the Centro Bicocca di Cosmologia Quantitativa (BiCoQ).

References

- Amaro-Seoane, P., Audley, H., Babak, S., et al. 2017, arXiv e-prints, arXiv:1702.00786
- Arcodia, R., Liu, Z., Merloni, A., et al. 2024, A&A, 684, A64
- Arcodia, R., Merloni, A., Nandra, K., et al. 2021, Nature, 592, 704
- Artymowicz, P., Lin, D. N. C., & Wampller, E. J. 1993, ApJ, 409, 592
- Bar-Or, B. & Alexander, T. 2016, ApJ, 820, 129
- Bondi, H. 1952, MNRAS, 112, 195
- Bonnerot, C. & Lu, W. 2020, MNRAS, 495, 1374
- Bonnerot, C., Lu, W., & Hopkins, P. F. 2021, MNRAS, 504, 4885
- Bortolas, E. 2022, MNRAS, 511, 2885
- Bortolas, E., Ryu, T., Broggi, L., & Sesana, A. 2023, MNRAS, 524, 3026
- Broggi, L. 2025, Phys. Rev. Lett., 135, 231201
- Broggi, L., Stone, N. C., Ryu, T., et al. 2024, The Open Journal of Astrophysics, 7, 48
- Chakraborty, J., Arcodia, R., Kara, E., et al. 2024, ApJ, 965, 12
- Chakraborty, J., Kara, E., Arcodia, R., et al. 2025, ApJ, 983, L39
- Chakraborty, J., Kara, E., Masterson, M., et al. 2021, ApJ, 921, L40
- Cohn, H. 1979, ApJ, 234, 1036
- Cohn, H. 1980, ApJ, 242, 765
- Cohn, H. & Kulsrud, R. M. 1978, ApJ, 226, 1087
- Curd, B. 2021, MNRAS, 507, 3207
- Dai, L. J., Fuerst, S. V., & Blandford, R. 2010, MNRAS, 402, 1614
- Dehnen, W. 1993, MNRAS, 265, 250
- Ferrarese, L. & Merritt, D. 2000, ApJ, 539, L9
- Franchini, A., Bonetti, M., Lupi, A., et al. 2023a, A&A, 675, A100

- Franchini, A., Bonetti, M., Lupi, A., et al. 2023b, *A&A*, 675, A100
- Gebhardt, K., Bender, R., Bower, G., et al. 2000, *ApJ*, 539, L13
- Giustini, M., Miniutti, G., & Saxton, R. D. 2020, *A&A*, 636, L2
- Goodman, J. & Tan, J. C. 2004, *The Astrophysical Journal*, 608, 108
- Gültekin, K., Richstone, D. O., Gebhardt, K., et al. 2009, *ApJ*, 698, 198
- Guolo, M., Pasham, D. R., Zajaček, M., et al. 2024, *Nature Astronomy*, 8, 347
- Hernández-García, L., Chakraborty, J., Sánchez-Sáez, P., et al. 2025, *Nature Astronomy* [arXiv:2504.07169]
- Hills, J. G. 1975, *Nature*, 254, 295
- Hopman, C. & Alexander, T. 2005, *ApJ*, 629, 362
- Izquierdo-Villalba, D., Sesana, A., Colpi, M., et al. 2024, *A&A*, 686, A183
- Karas, V. & Šubr, L. 2001, *A&A*, 376, 686
- Kaur, K., Rom, B., & Sari, R. 2024, in *Semi-Analytical Fokker Planck Models for Nuclear Star Clusters*
- Kaur, K., Stone, N. C., & Gilbaum, S. 2023, *MNRAS*, 524, 1269
- Kocsis, B., Yunes, N., & Loeb, A. 2011, *Physical Review D*, 84, 024032
- Levin, Y. 2003, arXiv e-prints, astro
- Levin, Y. 2007, *Monthly Notices of the Royal Astronomical Society*, 374, 515
- Linial, I. & Metzger, B. D. 2023, *The Astrophysical Journal*, 957, 34
- Lodato, G., Franchini, A., Bonnerot, C., & Rossi, E. M. 2015, *Journal of High Energy Astrophysics*, 7, 158
- Lodato, G. & Rossi, E. M. 2010, *Monthly Notices of the Royal Astronomical Society*, 410, 359
- Mancieri, D., Broggi, L., Bonetti, M., & Sesana, A. 2025a, *A&A*, 694, A272
- Mancieri, D., Broggi, L., Vinciguerra, M., Sesana, A., & Bonetti, M. 2025b, arXiv e-prints, arXiv:2509.02394
- Merritt, D. 2013, *Classical and Quantum Gravity*, 30, 244005
- Miller, M. C., Freitag, M., Hamilton, D. P., & Lauburg, V. M. 2005, *ApJ*, 631, L117
- Miniutti, G., Saxton, R. D., Giustini, M., et al. 2019, *Nature*, 573, 381
- Miniutti, G., Giustini, M., Arcodia, R., et al. 2023, *A&A*, 670, A93
- Mummery, A. & Balbus, S. A. 2020, *MNRAS*, 492, 5655
- Neumayer, N., Seth, A., & Böker, T. 2020, *The Astronomy and Astrophysics Review*, 28, 4
- Nicholl, M., Pasham, D. R., Mummery, A., et al. 2024, arXiv e-prints, arXiv:2409.02181
- Pan, X., Li, S.-L., Cao, X., Miniutti, G., & Gu, M. 2022, *The Astrophysical Journal Letters*, 928, L18
- Pan, Z. & Yang, H. 2021, *Phys. Rev. D*, 103, 103018
- Peters, P. C. 1964, *Physical Review*, 136, 1224
- Phinney, E. S. 1989, in *IAU Symposium, Vol. 136, The Center of the Galaxy*, ed. M. Morris, 543
- Piro, A. L. & Mockler, B. 2024, arXiv e-prints, arXiv:2412.01922
- Polkas, M., Bonoli, S., Bortolas, E., et al. 2024, *A&A*, 689, A204
- Quintin, E., Webb, N. A., Guillot, S., et al. 2023, *A&A*, 675, A152
- Qunbar, I. & Stone, N. C. 2024, *Phys. Rev. Lett.*, 133, 141401
- Raveh, Y. & Perets, H. B. 2021, *MNRAS*, 501, 5012
- Rees, M. J. 1988, *Nature*, 333, 523
- Rozner, M. & Ramirez-Ruiz, E. 2025, *The Astrophysical Journal Letters*, 988, L21
- Shen, R.-F. & Matzner, C. D. 2014, *The Astrophysical Journal*, 784, 87
- Śniegowska, M., Grzędzielski, M., Czerny, B., & Janiuk, A. 2023, *A&A*, 672, A19
- Spera, M., Giacobbo, N., & Mapelli, M. 2016, *Mem. Soc. Astron. Italiana*, 87, 575
- Spitzer, L. 1987, *Dynamical evolution of globular clusters*
- Stone, N. C., Vasiliev, E., Kesden, M., et al. 2020, *Space Sci. Rev.*, 216, 35
- Sun, H., Li, Y.-P., Pan, Z., & Yang, H. 2025, arXiv e-prints, arXiv:2509.00469
- Syer, D., Clarke, C. J., & Rees, M. J. 1991, *Monthly Notices of the Royal Astronomical Society*, 250, 505
- Tremaine, S., Richstone, D. O., Byun, Y.-I., et al. 1994, *AJ*, 107, 634
- Vasiliev, E. 2017, *ApJ*, 848, 10
- Vasiliev, E. & Merritt, D. 2013, *ApJ*, 774, 87
- Šubr, L. & Karas, V. 1999, *A&A*, 352, 452
- Wevers, T., Pasham, D. R., Jalan, P., Rakshit, S., & Arcodia, R. 2022, *A&A*, 659, L2
- Xian, J., Zhang, F., Dou, L., He, J., & Shu, X. 2021, *ApJ*, 921, L32
- Zhang, F. & Amaro Seoane, P. 2025, arXiv e-prints, arXiv:2510.10821
- Zhou, C., Zhong, B., Zeng, Y., Huang, L., & Pan, Z. 2024, *Phys. Rev. D*, 110, 083019